

Article

# Stability of a Flexible Asteroid Lander with Landing Control

Weifeng Yan , Ruoyu Feng  and Hexi Baoyin \*

School of Aerospace Engineering, Tsinghua University, Beijing 100084, China

\* Correspondence: baoyin@tsinghua.edu.cn

**Abstract:** Stable landing on asteroids is of considerable scientific and economic value but accompanied by huge difficulties. This paper proposes a novel flexible lander suitable for asteroids with microgravity and rugged surface. The gravity model with the artificial neural network and the surface model with the spherical harmonic method are introduced to establish the target asteroid's dynamical environment. The flexible dynamics with the discrete shell model, the collision with the spring-damping model and viscous sliding friction, and the rigid coupling with the constraint violation stabilization method are elaborated for the lander. Combining the asteroid's model with the lander's dynamics, one successful landing scenario of the lander is presented. The lander's landing stability of the final uncontrolled touching phase is studied through massive simulations. It is found that reasonable touching conditions can largely enhance the landing stability, and the lander can achieve a stable landing on the asteroid under a particular touching condition without control. The flexible lander's comparison to the rigid lander is also discussed. It is concluded that the flexible lander does have higher adaptability and lower risk in asteroid landing. What is more, the attitude controller and position controller for the lander's descent phase are also proposed and tested.

**Keywords:** asteroid exploration; flexible lander; landing stability; control



**Citation:** Yan, W.; Feng, R.; Baoyin, H. Stability of a Flexible Asteroid Lander with Landing Control. *Aerospace* **2022**, *9*, 719. <https://doi.org/10.3390/aerospace9110719>

Academic Editor: Fabio Ferrari

Received: 29 August 2022

Accepted: 10 November 2022

Published: 16 November 2022

**Publisher's Note:** MDPI stays neutral with regard to jurisdictional claims in published maps and institutional affiliations.



**Copyright:** © 2022 by the authors. Licensee MDPI, Basel, Switzerland. This article is an open access article distributed under the terms and conditions of the Creative Commons Attribution (CC BY) license (<https://creativecommons.org/licenses/by/4.0/>).

## 1. Introduction

Asteroid exploration is getting more and more attention due to its academic and economic value. It is widely recognized that some asteroids were born at the beginning of the solar system and therefore contained information about the solar system evolution [1,2], which is of great significance to planetary science. In addition, studies show that there exist rich rare metal resources on some asteroids [2]. With the development of deep space exploration, asteroids can be used as supply depots with abundant propulsion material.

With the development of aerospace technology and increasing interest in planetary protection, more and more asteroid exploration missions are being proposed and conducted. The exploration missions in the past can be roughly divided into circling exploration, short-range leap exploration, and landing exploration [3]. Landing exploration is a must to achieve comprehensive research about asteroids [4]. However, there exist a lot of difficulties in landing exploration. Different from planets with enough mass, asteroids' gravity is so weak that the lander is likely to rebound or escape even at a slow velocity. Additionally, the asteroids' terrain is usually rugged, which may cause the lander to overturn. The challenges above were first shown by the Philae lander, which tried but failed to stably land on Chury [5,6]. The Philae lander bounced for thousands of meters into a shaded crack after the failure of its anchoring harpoon system, and finally lost contact. In addition, the MINERVA-II and MASCOT landers of the Hayabusa2 mission also jumped for a long distance before their final stable landing [7,8]. Overall, the stable landing on asteroids is still tricky and worth further research.

Various feasible strategies for asteroid landing exploration have been proposed in past research. In the literature, there are several works that have focused on soft landing and in which asteroids' orbit dynamics and the control scheme have been discussed [9–12]. There have also been some works about landing exploration with a CubeSat-based lander, as

well as its simulation methods [13–18]. Some works have studied the improved anchoring method for asteroid landing based on Philae’s harpoon [19,20]. Recently, some researchers have noticed the unique advantages of flexible materials in asteroid landings. Some relevant works have focused on dissipating residual energy with flexible nets [21]; others have focused on the dynamical behavior of flexible materials in microgravity [4,22,23]. To expand on past research, this paper focuses on providing a feasible flexible lander of engineering significance for asteroid landing exploration, which should have both a flexible part to dissipate energy and a rigid part to carry out control and exploration. The asteroid flexible lander (shown in Figure 1) in this study is comprised of three rigid blocks connected with a thin layer of flexible materials, such as silicone rubber and vulcanized rubber. The necessary payloads, such as jets and the sampling instrument, are contained in the rigid blocks to conduct the control and sampling operations. When landing on the asteroid, the flexible lander will deform and dissipate energy via the deformation dissipation as well as the collision. Past research has indicated that the flexible structures can effectively avoid rebound and escape in weak gravity [4,21]. The symmetrical structure of the flexible lander can also avoid overturning on rugged terrain. Moreover, the symmetrical distribution and hexagonal prism shape of the blocks ensure that the blocks can be put together before the release phase to reduce space consumption, which is of great engineering significance. One asteroid landing mission can be divided into the launch of the exploration satellite, interplanetary transfer, orbital transfer to the target orbit, circling exploration, release of the lander, descent phase, and touching phase to the asteroid’s surface (see Figure 2). To avoid polluting the sampling area and damaging the lander during the landing, the jets are usually switched off after the descent phase, meaning the touching phase is uncontrolled. This paper mainly focuses on the touching phase, and the landing stability is discussed. In addition, a feasible controller for the descent phase is proposed and discussed briefly.

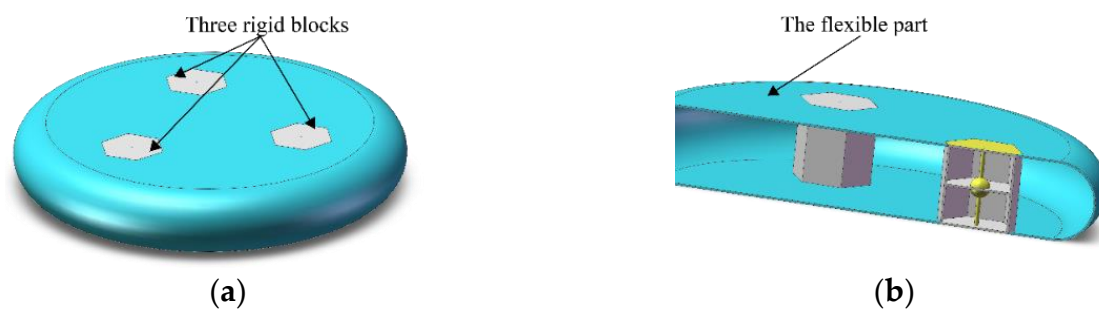


**Figure 1.** (a) The flexible asteroid landing lander; (b) the lander’s profile.

The main contributions of this paper can be summarized as follows. Firstly, this paper proposes an abstract physical model of a novel asteroid lander and develops the corresponding dynamical mode, including the asteroid’s dynamical model and the flexible landing dynamics, which are highly efficient and suitable for the flexible lander’s simulation. Secondly, this paper establishes the control scheme for the descent phase, in which reduced attitude equations are derived and the lander’s controllability is proved. Thirdly, this paper details the landing stability of the flexible lander for the touching phase, which gives accuracy requirements for the descent phase and shows the lander’s advantages in asteroid landing.

The rest of this paper is organized as follows. Section 2 establishes the asteroid’s dynamical environment, including the gravity and surface models. The following Section 3 details the flexible dynamics and the coupling dynamics of the flexible lander. Section 4 proposes a feasible controller for the descent phase for the flexible lander. Section 5 discusses one successful landing scenario, the landing stability of the proposed lander, the comparison to the rigid lander, and the simulation of the descent phase. Finally, the conclusion of this paper is given.

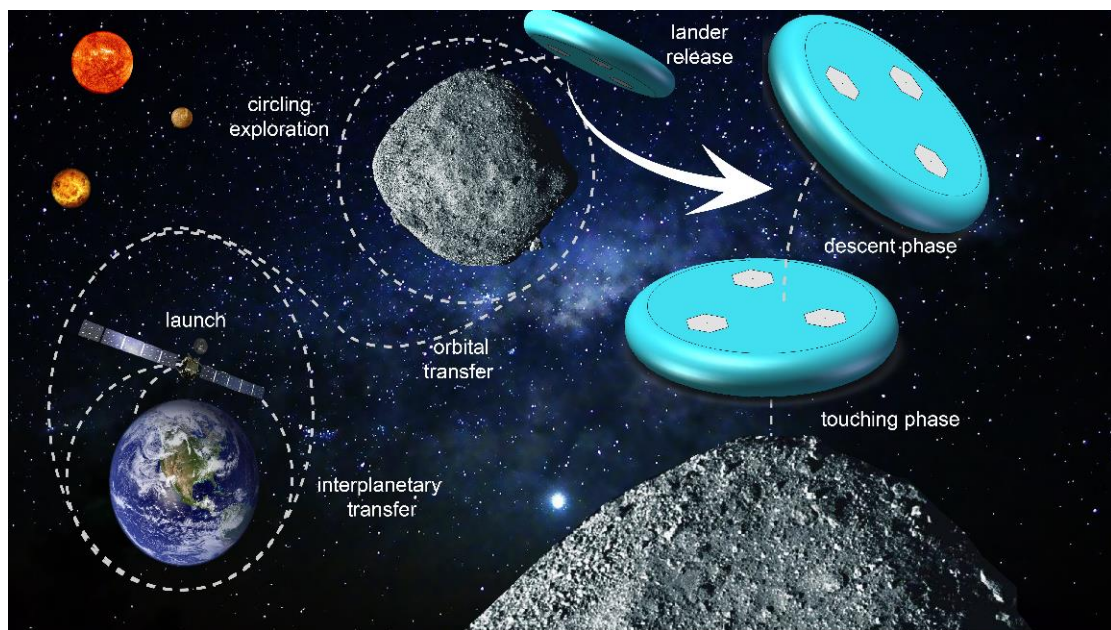


**Figure 2.** The concept of the asteroid exploration mission using the flexible lander.

## 2. Asteroid's Dynamical Environment

When exploring within the asteroid's Hill radius for a short term, only the asteroid's gravity and the collision need to be considered [24]. In this section, an efficient asteroid gravity model combining the artificial neural network (ANN) with the polyhedron method is proposed, and the asteroid surface model is also introduced.

### 2.1. Gravity Model

Asteroids usually have irregular shapes and mass distribution, which result in irregular gravity. To numerically model the asteroid's irregular gravity, Werner et al. [25] established the polyhedron method, which has high accuracy but low efficiency. Meanwhile, ANN can fit and predict complex functions with high efficiency and accuracy [26]. This paper adopts the polyhedron method to calculate the sample data for ANN and then predicts the asteroid's gravity.

The asteroid coordinate system is utilized, with the centroid as the origin, the minimum inertial axis as the  $x$  axis, the middle inertial axis as the  $y$  axis, and the maximum inertial axis as the  $z$  axis. In this coordinate system, the gravity is expressed as follows:

$$g(\mathbf{r}) = G\rho \sum_{f \in FS} \mathbf{F}_f \mathbf{r}_{fr} \omega_f - G\rho \sum_{e \in ES} \mathbf{E}_e \mathbf{r}_e L_e \quad (1)$$

where  $g(\mathbf{r})$  is the asteroid's gravity at position  $\mathbf{r}$ ,  $\rho$  is the asteroid's average density,  $FS$  represents all polyhedral units of the polyhedral model,  $ES$  stands for all edges of  $FS$ ,  $\mathbf{r}_{fr}$  is one vector from any point on  $f$  to the target point  $\mathbf{r}$ ,  $\mathbf{r}_e$  is one vector from any point on  $e$  to the target point,  $\mathbf{F}_f$  and  $\mathbf{E}_e$  are the tensors of  $f$  and  $e$ , respectively, and  $L_e$  and  $\omega_f$  are two dimensionless coefficients of the polyhedral units, as shown in ref [21,25].

This paper focuses on the gravity near the asteroid's surface, from which the sample data for the ANN are taken. Take Bennu as the target asteroid [27], whose size is  $565 \text{ m} \times 535 \text{ m} \times 508 \text{ m}$ . Accordingly, a ball with Bennu's centroid as the center and a radius of 500 m was chosen as the sample space. The sample point and its gravity calculated with the polyhedron method were set as the ANN's input and output, respectively. The number of sample data was 637,000, of which 90% were training data and 10% were validation data for the ANN; see Figure 3 for details.

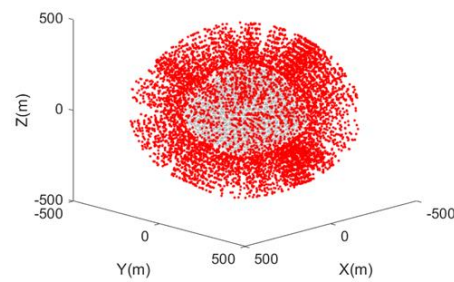


**Figure 3.** The distribution of sample points.

Factoring in accuracy and efficiency, the authors chose a network with 4 hidden layers and 256 nodes in each layer. The activation function for the input and output layers was the hyperbolic tangent (tanh). The activation function for the hidden layers was the rectified linear unit (ReLU). In the training, the learning rate was 0.0001, the batch case was 200, the training epoch was 60, and the training strategy was stochastic gradient descent with momentum (SGDM).

$f_{accuracy} = 1 - \frac{1}{N} \sum_{i=1}^N \|Net_g(\mathbf{r}_i) - \mathbf{g}(\mathbf{r}_i)\| / \|\mathbf{g}(\mathbf{r}_i)\|$  was adopted as the fitting accuracy to evaluate the ANN, where  $\mathbf{g}(\mathbf{r}_i)$  is the gravity at  $\mathbf{r}_i$ ,  $N$  means the number of sample data, and  $Net_g(\mathbf{r}_i)$  stands for the gravity calculated with ANN. After training, the fitting accuracy was 98.63%, which means a highly accurate prediction of the irregular gravity. Calculating 10,000 points' gravity in the same computer, the ANN took 0.16 s while the polyhedron method took 360.43 s, proving the ANN's great advantage in efficiency. What is more, the result of the ANN is an explicit continuous function, and therefore it is easy to be transplanted to other computing environments, and the gravitational gradient can also be estimated easily. Bennu's gravity calculated by the ANN is shown in Figure 4.

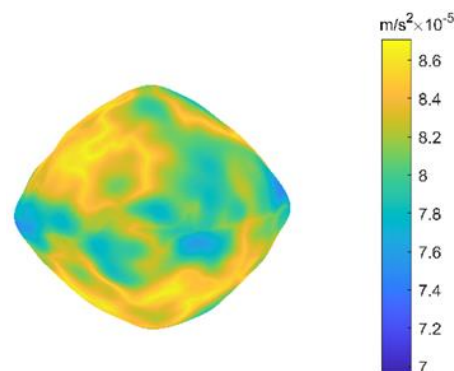


**Figure 4.** The learned gravity on Bennu's surface.

## 2.2. Surface Model

The asteroid's surface model is required when detecting the collision between the flexible lander and the asteroid. Usually, a polyhedron model is used to capture the asteroid's irregular shape, and reconstruction is used to obtain a continuous surface expression [13]. The spherical harmonic method is an efficient and mature reconstruction method that transforms the irregular surface into a series of spherical harmonics [28]. Here, this paper briefly introduces the spherical harmonic method.

The asteroid coordinate system mentioned above is utilized in this section. In this coordinate system, the formula for the spherical harmonic method is:

$$R(\theta, \varphi) = \sum_{n=0}^{\infty} \sum_{m=-n}^n C_n^m Y_n^m(\theta, \varphi) \quad \theta \in [0, \pi], \varphi \in [0, 2\pi] \quad (2)$$

where  $R(\theta, \varphi)$ ,  $\theta$ , and  $\varphi$  are the surface point's three components in the spherical coordinates, and  $C_n^m$  stands for the spherical harmonic complex coefficient, which can be calculated by the least square method with the surface data.  $Y_n^m(\theta, \varphi)$  represents the spherical harmonic basis function, and its formula is:

$$Y_n^m(\theta, \varphi) = \sqrt{\frac{2n+1}{4\pi} \cdot \frac{(n-m)!}{(n+m)!}} P_n^m(\cos \theta) e^{im\varphi} \quad (3)$$

where  $P_n^m(\cdot)$  is the Legendre polynomial; see Formula (4) for details:

$$P_n^m(\cos \theta) = \frac{(-1)^m}{2^n n!} (1 - \cos^2 \theta)^{m/2} \frac{d^{n+m}}{dx^{n+m}} (\cos^2 \theta - 1)^n \quad (4)$$

With Formulas (2)–(4), an explicit and continuous function for points on the asteroid's surface was obtained. The formula for the surface's local tangential and normal directions is:

$$\begin{cases} \tau_1 = \frac{\partial R}{\partial \theta} \hat{r} + R \frac{\partial \hat{r}}{\partial \theta} \\ \tau_2 = \frac{\partial R}{\partial \varphi} \hat{r} + R \frac{\partial \hat{r}}{\partial \varphi} \\ \lambda = \tau_1 \times \tau_2 \end{cases} \quad (5)$$

where  $\hat{r}$  is the unit vector from the origin to the surface point,  $\tau_1$  and  $\tau_2$  are two tangent vectors, and  $\lambda$  stands for the normal vector of the surface point; see [28] for details. Figure 5 shows the surface of Bennu reconstructed with the spherical harmonic method.

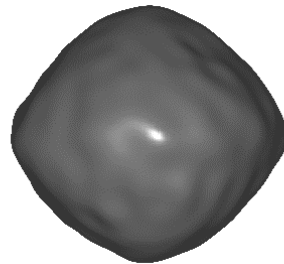


Figure 5. Bennu's reconstructed asteroid surface.

### 3. Flexible Landing Dynamics

There are flexible and rigid parts in the flexible lander. A shell characteristic exists in the flexible part, resulting in low computational efficiency when simulating with the finite element method or absolute node coordinate method. At the final landing on the asteroid, the collision between the lander and the asteroid's surface also needs to be taken into consideration. In this section, the discrete shell model suitable for the simulation of the flexible shell under large deformation is adopted. The tangential and normal collisions between the lander and the asteroid's surface are modeled, and the coupling dynamics for coupling the flexible and rigid parts are also introduced.

#### 3.1. Dynamics of the Flexible Part

The discrete shell model divides the flexible part along the middle plane into triangular units. The mass is assigned to the triangular units' vertex, called the mass point; see Figure 6 for details. The lander's movement is equivalent to the movement of the mass points during the simulation. It is worth noting that in this paper, the surface of the whole lander, including the rigid parts, is divided into units. The mass points corresponding to the rigid parts are fixed relative to the centroid through constraints. To describe the shell's deformation, the discrete shell model calculates the membrane energy and bending energy with the relative variation among units, and then obtains the inner forces with the two deformation energies [29–32].

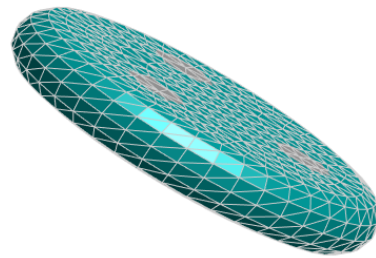


Figure 6. The units of the flexible lander.

When the flexible part deforms, one triangular unit’s membrane energy [31] is calculated by the following formula:

$$W_m = \frac{Eh}{2(1 - \mu^2)} \iint [\mu(\text{tr}\epsilon)^2 + (1 - \mu)\text{tr}\epsilon^2] dA \tag{6}$$

where  $W_m$  is the membrane energy for a deformed unit,  $E$  stands for Young’s modulus of the flexible material,  $h$  represents the thickness of the unit,  $\mu$  means the Poisson’s ratio of the flexible material,  $\text{tr}(\cdot)$  is the trace function, and  $\epsilon$  stands for the strain. According to ref [31],  $\text{tr}\epsilon$  and  $\text{tr}\epsilon^2$  can be rewritten as:

$$\begin{aligned} \text{tr}\epsilon &= \frac{(l_1^2 - L_1^2) \cot \alpha_1 + (l_2^2 - L_2^2) \cot \alpha_2 + (l_3^2 - L_3^2) \cot \alpha_3}{2A} \\ \text{tr}\epsilon^2 &= \frac{\sum_{i \neq j} 2\Delta^2 l_i \Delta^2 l_j - \sum_{i=1}^3 (\Delta^2 l_i)^2}{64A^2} \end{aligned} \tag{7}$$

where  $l_1, l_2,$  and  $l_3$  are the three side lengths of the deformed unit,  $L_1, L_2,$  and  $L_3$  represent the three side lengths of the undeformed unit,  $\alpha_1, \alpha_2, \alpha_3$  stand for the three angles of the undeformed unit,  $A$  is the area of the undeformed unit, and  $\Delta^2 l_i$  is equal to  $(l_i^2 - L_i^2)$ . More details about the symbols above are shown in Figure 7.

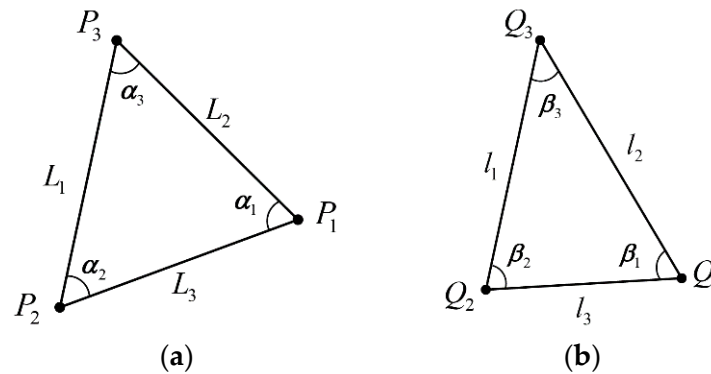


Figure 7. (a) The undeformed unit; (b) the deformed unit.

According to the Rayleigh-Ritz analysis, the inner force resulting from the membrane energy is the negative derivative of that membrane energy with respect to the positions of the unit’s mass points. The formula is:

$$F_{mi} = \sum_{j \neq i} [K_{ij}(l_k^2 - L_k^2) + K_i(l_j^2 - L_j^2) + K_j(l_i^2 - L_i^2)] (x_j - x_i) \tag{8}$$

where  $F_{mi}$  is the membrane inner force at point  $Q_i$  ( $i = 1, 2, 3$ ),  $(i, j, k)$  represents the non-repeated arrangement of  $(1, 2, 3)$ , and  $x_i$  stands for the position vector of  $Q_i$ .  $K_{ij}$  and  $K_i$  are constants related to the undeformed unit:

$$\begin{aligned} K_{ij} &= \frac{Eh(2 \cot \alpha_k + 1 - \mu)}{16(1 - \mu^2)A} \\ K_i &= \frac{Eh(2 \cot \alpha_j \cot \alpha_k + \mu - 1)}{16(1 - \mu^2)A} \end{aligned} \tag{9}$$

With Formulas (6)–(9), the membrane inner force caused by one deformed unit is derived. The total membrane inner force is obtained by summing the forces resulting from all deformed units. It is worth noting that only the units' side lengths and position vectors are required to update during the simulation, which ensures high computational efficiency.

When the flexible part deforms, the bending energy between two connected units [29] is calculated by the following formula:

$$W_b = \frac{Eh^3}{24(1 - \mu^2)} \frac{\|\bar{e}_0\|}{\bar{h}_e} (\bar{\theta}_e - \theta_e)^2 \tag{10}$$

where  $W_b$  is the bending energy for the two connected units,  $\theta_e$  is the angle between the two connected units with deformation,  $\bar{\theta}_e$  is the angle between the two connected units without deformation, and  $\|\bar{e}_0\|$  is the length of the undeformed common edge.  $\bar{h}_e$  is equal to  $(\bar{h}_{f0} + \bar{h}_{f1})/6$ , where  $\bar{h}_{f0}$  and  $\bar{h}_{f1}$  represent the undeformed heights of the two units on the common edge, respectively. See Figure 8 for more details about the symbols above.

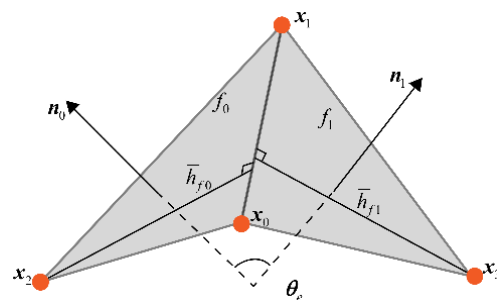


Figure 8. Illustration of the two connected units.

Like the membrane energy, the inner force resulting from the bending energy is the negative derivative of that bending energy with respect to the position of the unit's mass points. Noting that only  $\theta_e$  varies during the simulation, the formula is written as follows:

$$F_{bi} = -\frac{Eh^3}{12(1 - \mu^2)} \frac{\|\bar{e}_0\|}{\bar{h}_e} (\bar{\theta}_e - \theta_e) \frac{\partial \theta_e}{\partial x_i} \quad i = 0, 1, 2, 3 \tag{11}$$

where  $F_{bi}$  stands for the bending force on mass point  $x_i$ . According to ref [30],  $\partial \theta_e / \partial x_i$  is written as:

$$\begin{aligned} \frac{\partial \theta_e}{\partial x_0} &= -\frac{\cot \alpha_{03} \mathbf{n}_0 + \cot \alpha_{04} \mathbf{n}_1}{\|\bar{e}_0\|} \\ \frac{\partial \theta_e}{\partial x_1} &= -\frac{\cot \alpha_{01} \mathbf{n}_0 + \cot \alpha_{02} \mathbf{n}_1}{\|\bar{e}_0\|} \\ \frac{\partial \theta_e}{\partial x_2} &= \frac{\|\bar{e}_0\|}{2A_{f0}} \mathbf{n}_0 \\ \frac{\partial \theta_e}{\partial x_3} &= \frac{\|\bar{e}_0\|}{2A_{f1}} \mathbf{n}_1 \end{aligned} \tag{12}$$

where  $\alpha_{01}$  represents the angle between  $\vec{x}_0\vec{x}_1$  and  $\vec{x}_0\vec{x}_2$ ,  $\alpha_{02}$  stands for the angle between  $\vec{x}_0\vec{x}_1$  and  $\vec{x}_0\vec{x}_3$ ,  $\alpha_{03}$  is the angle between  $\vec{x}_1\vec{x}_0$  and  $\vec{x}_1\vec{x}_2$ ,  $\alpha_{04}$  represents the angle between  $\vec{x}_1\vec{x}_0$  and  $\vec{x}_1\vec{x}_3$ ,  $A_{f0}$  stands for the area of unit  $f_0$ , and  $A_{f1}$  means the area of unit  $f_1$ . The other symbols are the same as mentioned above.

Shells dissipate energy via bending oscillations [32]. Here, the dissipation force is given directly as a supplement to the bending force:

$$F_{ci} = -\frac{Eh^3\gamma}{12(1-\mu^2)} \frac{\|\bar{e}_0\|}{\bar{h}_e} \dot{\theta}_e \frac{\partial \theta_e}{\partial x_i} \tag{13}$$

where  $F_{ci}$  is the dissipation force on the mass point  $x_i$ , and  $\gamma$  is the dissipation coefficient, which is set as  $5 \times 10^{-4}$  in this paper.

By combining Formulas (10)–(13), the force resulting from bending is obtained. The total bending force is then obtained by calculating all two connected units. In each simulation step, only the  $\partial \theta_e / \partial x_i$  and  $\theta_e$  are recalculated, and therefore, high efficiency is ensured.

### 3.2. Collision Model

The landing exploration must consider the collision between the flexible model and the asteroid’s surface. A precise collision model will contribute a lot to the choices of the flexible material, landing site, and so on. In this study, the collision was equivalent to the normal and tangential interactions between the mass point and the surface. The spring-damping model based on the Hunt-Crossley theory and the Hertz model was adopted for the normal collision [4,33–35]. Such a collision model has been widely used in past research, so only the main equations are presented here. The formula for the normal collision is as follows:

$$F_n = (K_n d + C_n \dot{d}) \mathbf{n} \cdot \delta \tag{14}$$

where  $F_n$  is the normal collision force of the mass point, and  $d$  stands for the embedding depth of the mass point into the surface and is equal to  $R(\theta, \varphi) - \|r\|$ , where  $r$  is the mass point’s position vector.  $R(\theta, \varphi)$  means the asteroid surface distance to the origin with the same zenith angle and azimuth angle to the mass point; see Section 2.2 for details.  $\dot{d}$  is the component of the mass point’s velocity in the surface normal direction,  $\mathbf{n}$  is the unit normal vector of the asteroid surface, which is introduced in Section 2.2.  $\delta$  is the collision detection function; if  $d < 0$ ,  $\delta = 1$ , otherwise  $\delta = 0$ .  $K_n$  and  $C_n$  are the stiffness coefficient and damping coefficient from the Hertz model and Hunt-Crossley theory, respectively:

$$K_n = \frac{4}{3} \kappa^* E^* \tag{15}$$

$$C_n = -2 \sqrt{\frac{K_n m}{\pi^2 + (\ln e)^2}} \ln e$$

where  $m$  is the mass point’s mass,  $e$  means the coefficient of restitution,  $\kappa^*$  stands for the equivalent curvature radius between the mass point and the asteroid surface, and  $E^*$  represents the equivalent Young’s modulus. The formulas for  $\kappa^*$  and  $E^*$  are:

$$\kappa^* = \left( \frac{1}{\kappa_1} + \frac{1}{\kappa_2} \right)^{-0.5} \tag{16}$$

$$E^* = \left( \frac{(1-\mu_1^2)}{E_1} + \frac{(1-\mu^2)}{E} \right)^{-1}$$

where  $\kappa_1$  is the asteroid’s curvature radius at the collision point,  $\kappa_2$  means the mass point’s radius, which can be equivalent to a constant [21].  $E_1$  and  $\mu_1$  are the estimated Young’s modulus and Poisson’s ratio of material on the asteroid, and  $E$  and  $\mu$  represent Young’s modulus and Poisson’s ratio of the flexible material, respectively.

The viscous sliding friction was adopted for the tangential collision of the mass point and fully considers the asteroid surface’s characteristics. The formula is as follows:

$$F_t = \begin{cases} (\zeta F_n \cdot \mathbf{v}^\tau / \|\mathbf{v}^\tau\|) \delta, & K_t \|\mathbf{s}\| < \mu F_n \\ (K_t \mathbf{s} + C_t \mathbf{v}^\tau) \delta, & K_t \|\mathbf{s}\| \geq \mu F_n \end{cases} \tag{17}$$

where  $F_t$  stands for the force resulting from the tangential collision,  $\zeta$  means the coulomb friction coefficient,  $v^\tau$  is the mass point's velocity with respect to the collision point's tangential direction.  $\delta$  represents the collision detection function, as mentioned above.  $s$  stands for the mass point's slippage on the surface, which is equal to  $\int_{t_0}^t v^\tau dt$ , where  $t_0$  represents the start time of the collision.  $K_t$  is the tangential friction coefficient,  $C_t$  means the damping coefficient of the tangential frictions, which are considered to be equal to  $K_n/10$ , and  $C_n/100$ , respectively.

### 3.3. Coupling Dynamics

This paper presents the completed asteroid gravity model, the flexible dynamics for the flexible part, and the collision model. The coupling between the flexible and rigid parts was then solved with the constraint violation stabilization method [36]. In the asteroid coordinate system, the dynamical equation for the mass point  $i$  without connection to the rigid parts is:

$$m_i \ddot{r}_i = -m_i [2\omega \times \dot{r}_i + \omega \times (\omega \times r_i)] + m_i g(r_i) + (F_n^{(i)} + F_t^{(i)}) + F_i^{in} \tag{18}$$

where  $m_i$  is the mass of the mass point  $i$ ,  $r_i$  represents the position vector of the mass point,  $\omega$  stands for the asteroid's angular velocity,  $g(r_i)$  means the asteroid gravity,  $F_n^{(i)}$  and  $F_t^{(i)}$  are the normal and tangential collision forces on the mass point respectively, and  $F_i^{in}$  represents the inner force from the flexible part. The dynamical equations for the mass point  $j$  connected to the rigid parts are:

$$\begin{aligned} m_j \ddot{r}_j &= -m_j [2\omega \times \dot{r}_j + \omega \times (\omega \times r_j)] + m_j g(r_j) + (F_n^{(j)} + F_t^{(j)}) + F_j^{in} \\ \phi_j &= R_c(r_j - r_c) + C = 0 \end{aligned} \tag{19}$$

where  $\phi_j$  is the constraint on the mass point  $j$ ,  $\lambda_j$  is the Lagrange multiplier,  $r_c$  is the rigid parts' centroids,  $R_c$  represents the transformation matrix from the asteroid's ontology coordinate system to the rigid parts' ontology coordinate system, and  $C$  is a constant decided by the lander's undeformed state. The dynamical equations for the rigid part  $k$  are:

$$\begin{aligned} m_k \ddot{r}_k &= -m_k [2\omega \times \dot{r}_k + \omega \times (\omega \times r_k)] + m_k g(r_k) \\ \ddot{\Lambda}_k &= (R^T J R)^{-1} \left( \frac{1}{2} R^T M_r - 2R^T R \dot{R}^T J R \dot{\Lambda}_k \right) \\ \phi_k &= \Lambda_k^T \Lambda_k - 1 = 0 \end{aligned} \tag{20}$$

where  $\Lambda_k$  is the quaternion of the rigid part,  $J$  stands for the inertia matrix,  $M_r$  is the moment on the rigid part,  $\phi_k$  is the constraint for  $\Lambda_k$ , and  $R$  represents a  $3 \times 4$  matrix consisting of  $\Lambda_k$ ; see ref [37] for details.

The generalized coordinates  $q = [r_1 \ \cdots \ r_{Np} \ r_{c1} \ r_{c2} \ r_{c3} \ \Lambda_1 \ \Lambda_2 \ \Lambda_3]^T$  were adopted to rewrite Formulas (18)–(20), where  $Np$  is the number of the mass point,  $r_1 \ \cdots \ r_{Np}$  stands for the position vectors of all mass points, and  $[r_{c1} \ r_{c2} \ r_{c3} \ \Lambda_1 \ \Lambda_2 \ \Lambda_3]^T$  represent the position and attitude vectors of the three rigid parts. The rewritten formula is:

$$\begin{aligned} M \ddot{q} + \Phi_q^T \lambda &= F \\ \Phi &= 0 \end{aligned} \tag{21}$$

where  $M$  is the generalized mass matrix,  $F$  is the generalized force,  $\Phi$  is the vector consisting of all constraints, and  $\Phi_q^T$  is the transposed Jacobian matrix of  $\Phi$ . The constraint violation stabilization method solves Equation (21) as follows (see ref [38] for more details):

$$\begin{bmatrix} M & \Phi_q^T \\ \Phi_q & 0 \end{bmatrix} \begin{bmatrix} \ddot{q} \\ \lambda \end{bmatrix} = \begin{bmatrix} F \\ -(\Phi_q \dot{q})_q \dot{q} - 100 \dot{\Phi}_q - 2500 \Phi_q \end{bmatrix} \tag{22}$$

By solving the linear Equation (22), the generalized acceleration  $\ddot{\mathbf{q}}$  is solved. Combined with the initial condition, the lander’s movement over time is obtained via numerical integration.

#### 4. Control Scheme for the Descent Phase

In this section, the control scheme for the descent phase is proposed, which guides the flexible lander from the mother spacecraft to an appropriate state for the final touching phase. The corresponding simulation and test are set in Section 6.

##### 4.1. Attitude Control

The reduced attitude equations governing the flexible lander’s attitude and its control scheme are derived in this part. The complete attitude formula for the flexible lander is:

$$\tilde{\mathbf{I}}(t)\dot{\tilde{\boldsymbol{\omega}}} + \tilde{\boldsymbol{\omega}} \times (\tilde{\mathbf{I}}(t)\tilde{\boldsymbol{\omega}}) = \tilde{\mathbf{M}}_{\Sigma} \tag{23}$$

where  $\tilde{\mathbf{I}}(t)$  is the inertia matrix,  $\tilde{\boldsymbol{\omega}}$  is the angular velocity of the lander, and  $\tilde{\mathbf{M}}_{\Sigma}$  is the total moment from the control thruster and the environment. It is worth noting that  $\tilde{\mathbf{I}}(t)$  is not a constant matrix in the lander’s ontology coordinate system since the lander will deform during the motion. To reduce the difficulty in designing the control scheme, the deformation was not considered and the simplified attitude formula is as follows:

$$\mathbf{I}\dot{\boldsymbol{\omega}} + \boldsymbol{\omega} \times (\mathbf{I}\boldsymbol{\omega}) = \mathbf{M}_{\Sigma} \tag{24}$$

where  $\mathbf{I}$  represents the inertia matrix,  $\boldsymbol{\omega}$  is the angular velocity of the lander, and  $\mathbf{M}_{\Sigma}$  stands for the moment caused by the control thruster and the environment under the premise that the flexible lander will not deform, respectively. In the lander’s ontology coordinate system,  $\mathbf{I}$  and Formula (24) can be written as:

$$\mathbf{I} = \begin{bmatrix} I_{xx} & 0 & 0 \\ 0 & I_{yy} & 0 \\ 0 & 0 & I_{zz} \end{bmatrix} \tag{25}$$

$$\begin{aligned} I_{xx}\dot{\omega}_x &= (I_{zz} - I_{xx})\omega_y\omega_z + M_{cx} + M_{ex} \\ I_{yy}\dot{\omega}_y &= (I_{zz} - I_{yy})\omega_x\omega_z + M_{cy} + M_{ey} \\ I_{zz}\dot{\omega}_z &= M_{cz} + M_{ez} \end{aligned} \tag{26}$$

where  $I_{xx} = 134.58 \text{ kg/m}^2$ ,  $I_{yy} = 134.58 \text{ kg/m}^2$ , and  $I_{zz} = 73.81 \text{ kg/m}^2$  in this research,  $\omega_x$ ,  $\omega_y$ , and  $\omega_z$  are the three elements of  $\boldsymbol{\omega}$ ,  $\mathbf{M}_c = [M_{cx}, M_{cy}, M_{cz}]^T$  stands for the moment from the control thruster, and  $\mathbf{M}_e = [M_{ex}, M_{ey}, M_{ez}]^T$  means the moment from the environment.  $I_{xx}$ ,  $I_{yy}$ , and  $I_{zz}$  are the elements of  $\mathbf{I}$ , and  $I_{xx}$  is equal to  $I_{yy}$ , so  $\omega_z$  is the decoupling, as shown in Formula (26). As mentioned above,  $M_{cz}$  is equal to 0 if there is no deformation, and only the  $\omega_x$ ,  $\omega_y$  are controllable. According to ref [39], this study adopted the reduced attitude equations for the flexible lander, which means controlling a single unit vector of the attitude instead of controlling the whole attitude.

The equation governing the unit vector  $\mathbf{n} = [n_x, n_y, n_z]^T$ , which is expressed in the lander’s ontology coordinate system but fixed in the inertial system, is as follows:

$$\dot{\mathbf{n}} = -\boldsymbol{\omega} \times \mathbf{n} \tag{27}$$

where  $\|\mathbf{n}\| = 1$ . Combining Formula (26) with (27), and disregarding the environmental disturbance, the reduced attitude equations are proposed:

$$\begin{aligned} I_{xx}\dot{\omega}_x &= (I_{zz} - I_{xx})\omega_y\omega_z + M_{cx} + M_{ex} \\ I_{yy}\dot{\omega}_y &= (I_{zz} - I_{yy})\omega_x\omega_z + M_{cy} + M_{ey} \\ \dot{n}_x &= -\omega_y n_z + \omega_z n_y \\ \dot{n}_y &= \omega_x n_z - \omega_z n_x \end{aligned} \tag{28}$$

$\mathbf{x} = [\omega_x, \omega_y, n_x, n_y]^T - [\bar{\omega}_x, \bar{\omega}_y, \bar{n}_x, \bar{n}_y]^T$  was chosen as the state vector, where  $[\bar{\omega}_x, \bar{\omega}_y, \bar{n}_x, \bar{n}_y]^T$  represents the targeted state.  $\mathbf{u} = [M_x, M_y]$  was chosen as the input. Under the condition of one order of simplification, Formula (28) is derived into a linear time-invariant system:

$$\dot{\mathbf{x}} = A\mathbf{x} + B\mathbf{u} \quad (29)$$

$$A = \begin{bmatrix} 0 & \frac{I_{xx} - I_{zz}}{I_{xx}} \bar{\omega}_z & 0 & 0 \\ \frac{I_{zz} - I_{yy}}{I_{yy}} \bar{\omega}_z & 0 & 0 & 0 \\ 0 & -\bar{n}_z & 0 & \bar{\omega}_z \\ \bar{n}_z & 0 & \bar{\omega}_z & 0 \end{bmatrix}, B = \begin{bmatrix} 0 & \frac{1}{I_{xx}} \\ \frac{1}{I_{yy}} & 0 \\ 0 & 0 \\ 0 & 0 \end{bmatrix}$$

By checking the controllability matrix's rank, it is easy to find that when  $\bar{n}_z \neq 0$ , the system is controllable. Considering the time invariance of the attitude equation and that  $\bar{n}_z$  is designable, it can be concluded that the flexible lander's reduced attitude is controllable. With Equation (29), the controller can be easily designed by using the linear-quadratic regulator (LQR) method. LQR is a traditional and mature method for the linear time-invariant system, and therefore, this paper does not discuss it deeply [40]. The descent simulation with the LQR controller is discussed in the following section. With the attitude controller,  $\mathbf{n}$  is controllable to the target, which means that the lander's attitude is controllable.

#### 4.2. Position Control

The position controller was designed under the premise that the flexible lander will not deform, and the lander's normal direction is controllable since the thrust of the proposed lander is along the lander's normal direction. A feasible control is that the response time of the attitude controller is much shorter than the position controller to ensure an appropriate thrust direction.

This study adopted the PID controller for the position control, which makes the lander's ideal acceleration  $\ddot{\mathbf{d}}_{des}$  as a second-order system, as shown in Formula (30).

$$\ddot{\mathbf{d}}_{des} + 2\eta\omega_n\dot{\mathbf{d}} + \omega_n^2\mathbf{d} = 0 \quad (30)$$

where  $\mathbf{d}$  stands for the vector from the lander to the target point,  $\eta$  is the damping ratio, and  $\omega_n$  represents the natural frequency of the PID controller. The total thrust  $f_\Sigma$  is derived as follows:

$$f_\Sigma = m\mathbf{n}_{des} \cdot \ddot{\mathbf{d}}_{des} \quad (31)$$

where  $m$  is the total mass of the lander, and  $\mathbf{n}_{des}$  stands for the instantaneous normal direction of the lander.

Combining the input  $\mathbf{u} = [M_x, M_y]$  of the attitude controller and the total thrust  $f_\Sigma$  of the position controller, the thrust  $f_1, f_2, f_3$  that the three thrusters should produce during the descent phase is as follows:

$$\begin{bmatrix} M_x \\ M_y \\ f_\Sigma \end{bmatrix} = \begin{bmatrix} 0 & -l/2 & l/2 \\ l/\sqrt{3} & -l/2\sqrt{3} & l/2\sqrt{3} \\ 1 & 1 & 1 \end{bmatrix} \begin{bmatrix} f_1 \\ f_2 \\ f_3 \end{bmatrix} \quad (32)$$

where  $l$  means the distance between each two rigid parts' centroid when the lander is not deformed.

### 5. Landing Simulation and Discussions

This paper presents the completed method for simulating asteroids' dynamic environments and the motion of the flexible lander, which contributes to the foundation for the landing simulation of the asteroid. In this section, a successful landing scenario on the asteroid, the landing stability of the flexible lander, and the comparison between the

flexible lander and the rigid lander are presented and discussed. The simulation of the descent phase is also shown in this section.

### 5.1. Stable Landing Scenario

This section presents one successful landing of the flexible lander, demonstrating its feasibility. The asteroid Bennu was chosen as the landing target, which was also the target of NASA's OSIRIS-Rex. The material with a Young's modulus of 0.001 GPa, a Poisson's ratio of 0.4, and a density of  $1000 \text{ kg/m}^3$  was chosen as the flexible part's material, which corresponds to the silicone rubber. The thickness of the flexible part was 0.005 m and the total mass of the flexible material was 53.19 kg. The mass and the moment of inertia for three rigid parts were all set as 150 kg and  $\text{diag}([10 \ 10 \ 10]) \text{ kg/m}^3$ , respectively. The initial center of the flexible lander was located at  $[13 \ -13 \ 255]^T \text{ m}$ , the initial attitude quaternion between the asteroid's ontology coordinate system and the lander's ontology coordinate system was  $[0.9582 \ 0 \ 0.2860 \ 0]^T$ , and the initial speed was  $[0.0199 \ 0 \ -0.0980]^T \text{ m/s}$ . Under the above conditions, the first collision happened at  $[13.3 \ -13.0 \ 253.6]^T \text{ m}$ , which is a relatively flat area on the Bennu, and therefore was chosen as an ideal landing point in this study. The whole simulation time was 2000 s.

It is difficult to use the lander's centroid to describe the movement due to its deformation during the collision, so this study adopted the centroid of the three rigid parts instead. Figure 9a,b shows the trajectory of the flexible lander on the asteroid. Figure 9c,d shows the flexible lander at 17 s and 2000 s, respectively. Figure 10 shows the variation in the distance between the center of the lander and the targeted landing site.

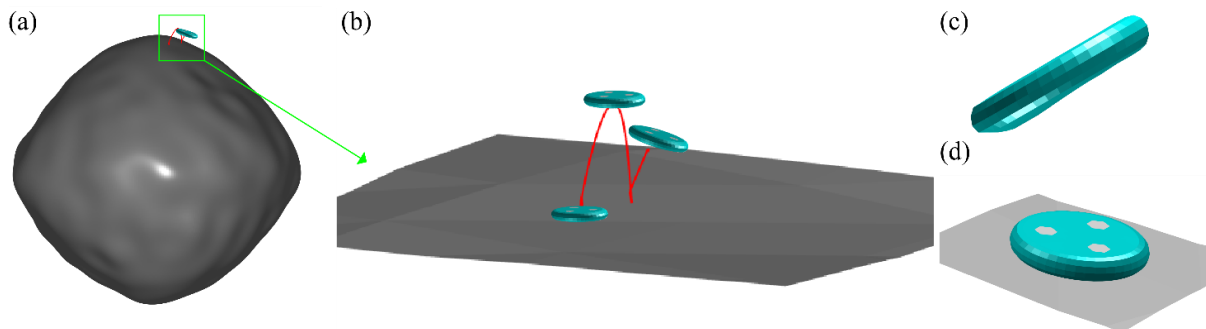


**Figure 9.** (a) The flexible lander on the asteroid; (b) the movement of the flexible lander on the asteroid; (c) the first collision at 17 s; (d) the flexible lander completing a stable landing.

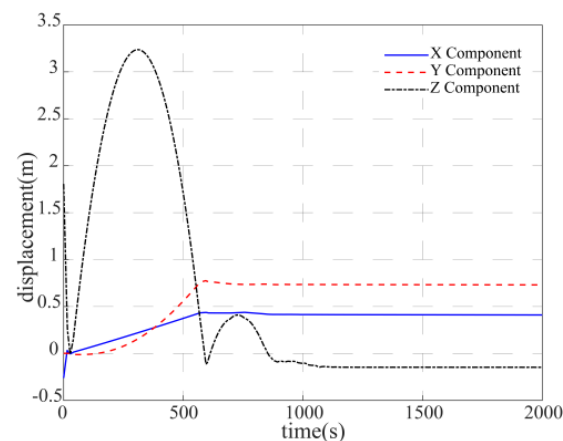


**Figure 10.** The distance between the flexible lander and the targeted landing site.

Figures 9 and 10 show that with the conditions above, the first collision happened at 17 s, during which the flexible lander deformed obviously, as shown in Figure 9c, and

its energy dissipated through the collision and deformation. The asteroid's gravity was so weak that the lander could not achieve a stable landing through one collision. After the first collision, the lander moved in the form of a parabola under the microgravity and collided with the asteroid at 596 s again. The lander returned to the asteroid's surface and then bounced several times after the second collision. The lander finally achieved a stable landing, as shown in Figure 9d. During a series of collisions, the lander did not leave the target point too far during the whole landing, and the final distance between the lander and the target point was just 0.8506 m, which shows the potential of the flexible lander in avoiding rebound and escape under microgravity. See Figures 9 and 10 for more details.

All in all, the flexible lander completed a stable landing on the asteroid through passive deformation in the uncontrolled touching phase.

### 5.2. Landing Stability of the Flexible Lander

This section focuses on the flexible lander's landing stability through massive simulations, guiding the touching condition of the lander. Too many factors affect the lander's landing, such as the lander's attitude, the uneven surface, etc. Taking so many factors into account is impossible, and therefore this study focused on three main elements, which are the flexible lander's initial velocity  $v_0$ , the angle  $\beta$  between the ground and the velocity, and the angle  $\alpha$  between the ground and the lander. The three elements are also the main control variables in the practical touching of the asteroid lander, as shown in Figure 11. In this section, the rugged terrain is not considered as a main research factor since a flat area is normally chosen for landing in practice. In microgravity, the influence of rugged terrain and the error in observation of the asteroid's surface can be equivalent to the errors of  $\alpha$  and  $\beta$ . The irregular asteroid's gravity is also assumed to be constant since the primary component of the gravity changes little on the asteroid's surface, especially on the asteroid Bennu, which is close to spherical.

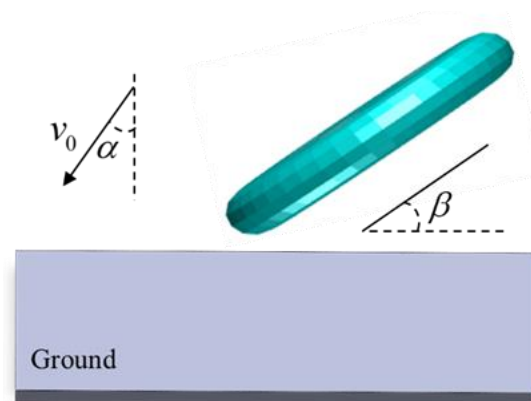


**Figure 11.** Illustration of the simulation conditions.

The rebound distance between the targeted landing site and the next touching point was considered to be the index for the landing stability. This study took 5 m as the criterion for a stable landing. In the simulation,  $v_0$  was set as 0.1 ~ 0.3 m/s,  $\alpha$  was set as  $-45^\circ \sim 45^\circ$ ,  $\beta$  was set as  $-45^\circ \sim 45^\circ$ , the parameters of the flexible lander were set as mentioned in Section 5.1, and the gravity was set as  $[0 \ 0 \ 8 \times 10^{-5}] \text{ m/s}^2$ , which is an estimate of the mean gravity on Bennu's surface. Figure 12a–c illustrates the lander's tangential velocity, normal velocity after the first collision, and its rebound distance in the condition of  $v_0 = 0.1 \text{ m/s}$ , respectively. Local amplification of Figure 12c is shown in Figure 12d,e. Figure 12f illustrates the lander's rebound distance in the condition of  $v_0 = 0.2 \text{ m/s}$ . Figure 12g illustrates the lander's rebound distance in the condition of  $v_0 = 0.3 \text{ m/s}$ . The red contour in Figure 12c,f,g marks the feasible scope of  $\alpha$  and  $\beta$  for a stable landing using the mentioned criterion. It is worth noting that the lander's rebound

distance in this study was solved by assuming the lander's movement as a parabola with its tangential and normal velocity so as to reduce the simulation time.

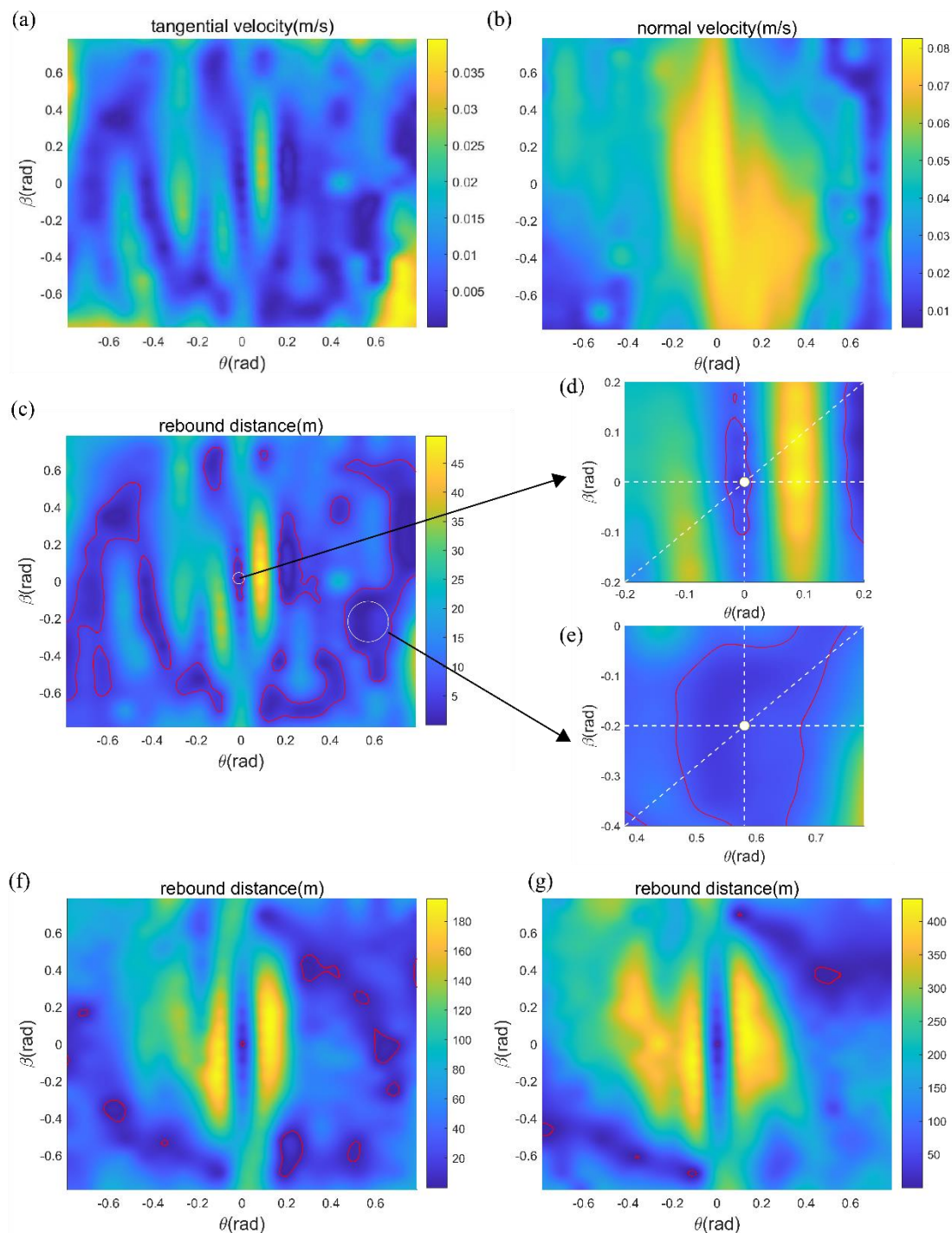


**Figure 12.** (a) The flexible lander's tangential velocity after the first collision at  $v_0 = 0.1$  m/s ; (b) the flexible lander's normal velocity after the first collision at  $v_0 = 0.1$  m/s; (c) the flexible lander's rebound distance at  $v_0 = 0.1$  m/s; (d) local amplification of the origin in Figure 4c; (e) local amplification of  $\alpha = 0.58$ ,  $\beta = -0.2$  in Figure 4c; (f) the flexible lander's rebound distance at  $v_0 = 0.2$  m/s; (g) the flexible lander's rebound distance at  $v_0 = 0.3$  m/s.

Figure 12 shows that  $v_0$ ,  $\alpha$ , and  $\beta$  significantly impacted the landing, proving the necessity of this research. Here, this paper presents a detailed discussion of Figure 12a–e, which corresponds to  $v_0 = 0.1$  m/s. From Figure 12a, it can be concluded that the smaller

$\alpha$  and  $\beta$  are, the larger the normal velocity will be, which brings more escaping risk to a landing. In Figure 12b, there is an opposite trend in the tangential velocity, so  $\alpha$  and  $\beta$  will be neither too small nor too large. In Figure 12c, it is easy to find that a stable landing only happens in some areas of  $\alpha$  and  $\beta$ . Reasonable  $\alpha$  and  $\beta$  values can enhance the flexible lander's adaptability on the asteroid through higher energy dissipation, while a wrong touching condition of the lander will cause a long-rebound distance. When landing under the conditions of  $v_0 = 0.1$  m/s,  $\alpha = 0$ , and  $\beta = 0$ , the allowable errors in  $\alpha$ ,  $\beta$ , and terrain slopes are  $(-0.03, 0.01)$ ,  $(-0.12, 0.14)$ , and  $(-0.03, 0.01)$ , respectively, as illustrated in Figure 4d. When landing under the state of  $v_0 = 0.1$  m/s,  $\alpha = 0.58$ , and  $\beta = -0.2$ , corresponding to the initial condition in Section 5.1, the allowable errors in  $\alpha$ ,  $\beta$ , and terrain slopes are  $(-0.12, 0.11)$ ,  $(-0.23, 0.17)$ , and  $(-0.12, 0.15)$ , respectively, which means much better adaptability on the asteroid, as seen in Figure 12e.  $\alpha = 0$  and  $\beta = 0$  are usually chosen when landing on planets with larger gravity. However, this is not an appropriate choice under the microgravity of the flexible lander. Under the condition of  $v_0 = 0.2$  m/s, the feasible scopes of  $\alpha$  and  $\beta$  are much smaller than that of  $v_0 = 0.1$  m/s, as shown in Figure 12f. When  $v_0 = 0.3$  m/s, a stable landing is nearly impossible, as seen in Figure 12g. It is evident that the higher the  $v_0$  is, the lower the possibility of a successful landing is, which is also reflected in these results.

### 5.3. Comparison with the Rigid Lander

This section discusses the flexible lander's comparison with the rigid lander, showing the flexible lander's potential advantage in asteroid exploration. The simulation was almost the same as that in Section 5.2, and only the material of the lander's flexible part was substituted with steel with a Young's modulus of 201 GPa and a Poisson's ratio of 0.4. The rigid lander's deformation was negligible with this stiffness. Figure 13a–c shows the rigid lander's tangential velocity, the normal velocity after the first collision, and its rebound distance under the condition of  $v_0 = 0.1$  m/s, respectively. Figure 13d,e shows the local amplification of the origin and the best  $\alpha$  and  $\beta$ , respectively.

Compared to Figure 12, it was found that the rigid lander's feasible scopes for  $\alpha$  and  $\beta$  at  $v_0 = 0.1$  m/s were much smaller than the flexible lander, meaning more risk in landing. The longest rebound distance was nearly double the flexible lander's, indicating more divergence to the targeted landing site. The sensitivity to  $\alpha$  and  $\beta$  are also remarkable for the rigid lander, showing the significance of this research. When landing under the conditions of  $v_0 = 0.1$  m/s,  $\alpha = 0$ , and  $\beta = 0$ , the allowable errors in  $\alpha$ ,  $\beta$ , and the terrain slopes are  $(-0.02, 0.02)$ ,  $(-0.38, 0.38)$ , and  $(-0.02, 0.02)$ , respectively, as seen in Figure 13d. When landing under the conditions of  $v_0 = 0.1$  m/s,  $\alpha = 0.22$ , and  $\beta = -0.66$ , which are better touching conditions for the rigid lander, the allowable errors in  $\alpha$ ,  $\beta$ , and the terrain slopes are  $(-0.23, 0.08)$ ,  $(-0.07, 0.06)$ , and  $(-0.08, 0.10)$ , respectively, meaning a higher possibility of a stable landing than landing under the conditions of  $v_0 = 0.1$  m/s,  $\alpha = 0$ , and  $\beta = 0$ , as seen in Figure 13e. Comparing the aforementioned results for the flexible and rigid lander, it is clear that the flexible lander had better adaptability on the uneven terrain and lower requirements for control.

In conclusion, the flexible lander does have an edge in asteroid landing.

### 5.4. Simulation of the Descent Phase

A feasible controller for the descent phase has been proposed above in theory. This section applies the controller to the flexible lander to prove its feasibility.

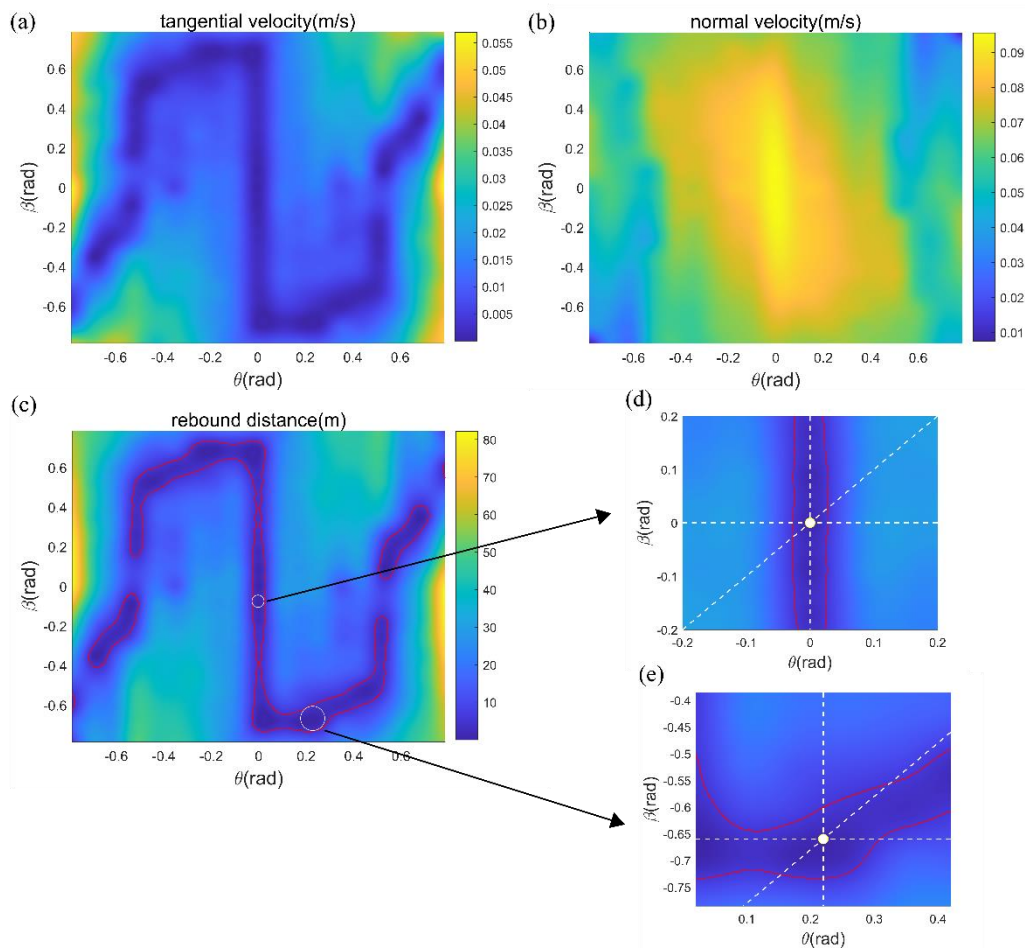


**Figure 13.** (a) The rigid lander’s tangential velocity after the first collision at  $v_0 = 0.1$  m/s; (b) the rigid lander’s normal velocity after the first collision at  $v_0 = 0.1$  m/s; (c) the rigid lander’s rebound distance at  $v_0 = 0.1$  m/s; (d) local amplification of the origin in (c); (e) local amplification of  $\alpha = 0.22$ ,  $\beta = -0.66$  in (c).

In the simulation, this study assumed that the three rigid parts’ position and velocity were measured in real-time, and the state vector needed by the controller was estimated accordingly. The weighted matrices  $Q$  and  $R$  of the LQR controller were both set as the unital matrix. The PID controller’s damping ratio and natural frequency were set to 2 and 0.01, respectively. In the beginning, the flexible lander was located at  $[0 \ 0 \ 280]^T$  m, the initial attitude quaternion between the asteroid’s ontology coordinate system and the lander’s ontology coordinate system was  $[1 \ 0 \ 0 \ 0]^T$ , and the initial speed was  $[0 \ 0 \ 0]^T$  m/s. The target point was  $[2 \ 2 \ 288]^T$  m, and  $[0.2357 \ 0.2357 \ 0.9428]^T$  was chosen as target  $n$ . The parameters of the flexible lander were set as mentioned in Section 5.1. The simulation lasted for 1000 s, and the attitude controller began working at  $t = 0$  s while the position controller began working at  $t = 100$  s.

Figure 14 shows the distance between the lander and the target point, as well as the angle between the lander’s normal direction and the target  $n$ . The lander’s normal direction was calculated according to the three rigid parts’ position in case the lander deformed during the control. Figure 14 shows that the controller could control the flexible lander to the target point with centimeter position accuracy, and its normal direction to the target direction had nearly 0 attitude error above the asteroid.

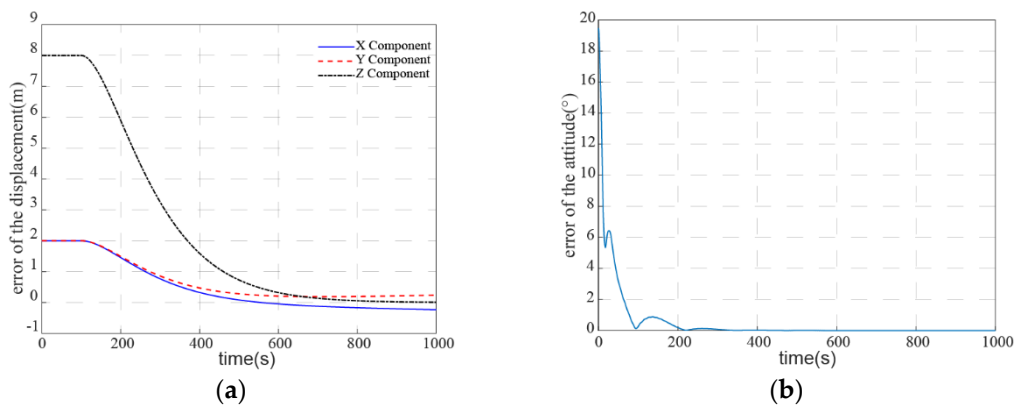


**Figure 14.** (a) The distance between the flexible lander and the target; (b) the angle between the lander's normal direction and the target  $n$ .

In conclusion, the controller is feasible for the descent phase.

## 6. Conclusions

In this work, a novel flexible asteroid lander is proposed, and the corresponding dynamics, including the asteroid's dynamical environment, the flexible dynamics, and the coupling dynamics, are established. Taking Bennu as the target asteroid, simulations of the final touching phase were performed and discussed, of which one successful stable landing scenario is shown, the landing stability is detailed, and the comparison to the rigid lander is presented. It is concluded that reasonable touching conditions can enhance the flexible lander's adaptability, and the flexible lander has better stability as well as lower requirements for control than a rigid lander. Furthermore, the controller for the descent phase was designed, and a corresponding simulation was conducted. The results of the simulation show that the controller is feasible and the touching condition is controllable with the controller. To expand on this research, it will be valuable to consider an optimum design of the flexible lander, including the thickness of the flexible material and the distribution of the rigid blocks. Designing an experimental prototype and test beds to simulate the asteroid's dynamical environment is also significant for future research. In addition, an optimal controller for the descent phase is worth further study.

**Author Contributions:** Investigation, methodology, software, writing—original draft, W.Y.; methodology, software, writing—review and editing, R.F.; methodology, project administration, writing—review and editing, H.B. All authors have read and agreed to the published version of the manuscript.

**Funding:** This research was funded by the National Key R&D Program of China, grant number 2019YFA0706500.

**Institutional Review Board Statement:** Not applicable.

**Informed Consent Statement:** Not applicable.

**Data Availability Statement:** Not applicable.

**Conflicts of Interest:** The authors declare no conflict of interest.

## References

- Castillo-Rogez, J.C.; Pavone, M.; Nesnas, I.; Hoffman, J.A. Expected science return of spatially-extended in-situ exploration at small Solar system bodies. In Proceedings of the Aerospace Conference, Big Sky, MT, USA, 3–10 March 2012.
- Peloni, A.; Ceriotti, M.; Dachwald, B. Solar-Sail Trajectory Design for a Multiple Near-Earth-Asteroid Rendezvous Mission. *J. Guid. Control Dyn. A Publ. Am. Inst. Aeronaut. Astronaut. Devoted Technol. Dyn. Control* **2016**, *39*, 2712–2724. [[CrossRef](#)]
- Luo, Y.; Jiang, X.; Zhong, S.; Ji, Y.; Sun, G. Multisatellite Task Allocation and Orbit Planning for Asteroid Terminal Defence. *Aerospace* **2022**, *9*, 364. [[CrossRef](#)]
- Yan, W.; Baoyin, H. A Numerical Research on a New Type of Asteroid Flexible Probe. *IEEE Access* **2021**, *9*, 129863–129873. [[CrossRef](#)]

5. Dorofeeva, V.A. Chemical and Isotope Composition of Comet 67P/ChuryumovGerasimenko: The RosettaPhilae Mission Results Reviewed in the Context of Cosmogony and Cosmochemistry. *Sol. Syst. Res.* **2020**, *54*, 96–120. [[CrossRef](#)]
6. Hand, E. Philae probe makes bumpy touchdown on a comet. *Science* **2014**, *346*, 900–901. [[CrossRef](#)]
7. Yoshikawa, M.; Kawaguchi, J.; Kuninaka, H. The Results of Asteroid Exploration Mission Hayabusa. *Ieice Tech. Rep.* **2010**, *110*, 219–222.
8. Fujiwara, A.; Kawaguchi, J.; Yeomans, D.; Abe, M.; Mukai, T.; Okada, T.; Saito, J.; Yano, H.; Yoshikawa, M.; Scheeres, D. The rubble-pile asteroid Itokawa as observed by Hayabusa. *Science* **2006**, *312*, 1330–1334. [[CrossRef](#)]
9. Li, X.; Qiao, D.; Huang, J.; Han, H.; Meng, L. Dynamics and control of proximity operations for asteroid exploration mission. *Sci. China Phys. Mech. Astron.* **2019**, *49*, 084508. (In Chinese) [[CrossRef](#)]
10. Tang, G.; Jiang, F.; Li, J. Low-thrust trajectory optimization of asteroid sample return mission with multiple revolutions and moon gravity assists. *Sci. China Phys. Mech. Astron.* **2015**, *58*, 114501. [[CrossRef](#)]
11. Chen, Y.; Baoyin, H.; Li, J. Design and optimization of a trajectory for Moon departure Near Earth Asteroid exploration. *Sci. China Phys. Mech. Astron.* **2011**, *54*, 748–755. [[CrossRef](#)]
12. Huang, J.; Li, X.; Qiao, D.; Jia, F.; Meng, L. Mission design for multi-target and multi-mode rendezvous missions to small bodies. *Sci. China Phys. Mech. Astron.* **2019**, *49*, 084512. (In Chinese) [[CrossRef](#)]
13. Wal, S.V.; Reid, R.G.; Scheeres, D.J. Simulation of Nonspherical Asteroid Landers: Contact Modeling and Shape Effects on Bouncing. *J. Spacecr. Rocket.* **2019**, *57*, 1–22.
14. Bazzocchi, M.C.; Hakima, H. A CubeSat-based Robotic Asteroid Sampling Mission. In Proceedings of the AIAA Scitech 2020 Forum, Orlando, FL, USA, 6–10 January 2020.
15. Kim, Y.-B.; Jeong, H.-J.; Park, S.-M.; Lim, J.H.; Lee, H.-H. Prediction and Validation of Landing Stability of a Lunar Lander by a Classification Map Based on Touchdown Landing Dynamics' Simulation Considering Soft Ground. *Aerospace* **2021**, *8*, 380. [[CrossRef](#)]
16. Zhang, Y.; Li, J.; Zeng, X.; Wen, T.; Li, Z. High-fidelity landing simulation of small body landers: Modeling and mass distribution effects on bouncing motion. *Aerosp. Sci. Technol.* **2021**, *119*, 107149. [[CrossRef](#)]
17. Wen, T.; Zeng, X.; Circi, C.; Gao, Y. Hop reachable domain on irregularly shaped asteroids. *J. Guid. Control Dyn.* **2020**, *43*, 1269–1283. [[CrossRef](#)]
18. Zen, X.; Li, Z.; Gan, Q.; Circi, C. Numerical study on the low-velocity impact of the asteroid lander onto deformable regolith surfaces. *J. Guid. Control Dyn.* **2022**, *45*, 1644–1660.
19. Zhao, Z.; Zhao, J.; Hong, L. An asteroid landing mechanism and its landing simulation. In Proceedings of the 2012 IEEE International Conference on Robotics and Biomimetics (ROBIO), Guangzhou, China, 11–14 December 2012.
20. Wang, Y.; Jiang, W.; Long, L.; Zhu, Q.; Feng, R.; Wang, L.; Antonio, C. Design and Experimental Research of a New Type of Asteroid Anchoring System. *Int. J. Aerosp. Eng.* **2021**, *2021*, 1–7.
21. Zhang, Y.; Yu, Y.; Baoyin, H. Dynamical behavior of flexible net spacecraft for landing on asteroid. *Astrodynamics* **2021**, *5*, 249–261. [[CrossRef](#)]
22. Bartlett, N.W.; Tolley, M.T.; Overvelde, J.T.B.; Weaver, J.C.; Mosadegh, B.; Bertoldi, K.; Whitesides, G.M.; Wood, R.J. A 3D-printed, functionally graded soft robot powered by combustion. *Science* **2015**, *349*, 161–165. [[CrossRef](#)]
23. Feng, R.; Zhang, Y.; Liu, J.; Zhang, Y.; Li, J.; Baoyin, H. Soft Robotic Perspective and Concept for Planetary Small Body Exploration. *Soft Robot.* **2022**, *9*, 889–899. [[CrossRef](#)]
24. Hamilton, D.P.; Burns, J.A. Orbital stability zones about asteroids. *Icarus* **1991**, *92*, 118–131. [[CrossRef](#)]
25. Werner, R.A.; Scheeres, D.J. Exterior gravitation of a polyhedron derived and compared with harmonic and mascon gravitation representations of asteroid 4769 Castalia. *Celest. Mech. Dyn. Astron.* **1996**, *65*, 313–344. [[CrossRef](#)]
26. Song, Y.; Cheng, L.; Gong, S. Fast estimation of gravitational field of irregular asteroids based on deep learning and its applications. In Proceedings of the 29th AAS/AIAA Space Flight Mechanics Meeting, Maui, HI, USA, 13–17 January 2019.
27. Chesley, S.R.; Farnocchia, D.; Nolan, M.C.; Vokrouhlický, D.; Chodas, P.W.; Milani, A.; Spoto, F.; Rozitis, B.; Benner, L.A.; Bottke, W.F.; et al. Orbit and bulk density of the OSIRIS-REx target Asteroid (101955) Bennu. *Icarus* **2014**, *235*, 5–22. [[CrossRef](#)]
28. Yu, Y.; Michel, P.; Hirabayashi, M.; Schwartz, S.R.; Zhang, Y.; Richardson, D.C.; Liu, X. The Dynamical Complexity of Surface Mass Shedding from a Top-shaped Asteroid Near the Critical Spin Limit. *Astron. J.* **2018**, *156*, 59. [[CrossRef](#)]
29. Grinspun, E. *A Discrete Model of Thin Shells*; Birkhäuser: Basel, Switzerland, 2005.
30. Wardetzky, M.; Bergou, M.; Harmon, D.; Zorin, D.; Grinspun, E. Discrete quadratic curvature energies. *Comput. Aided Geom. Des.* **2007**, *24*, 499–518. [[CrossRef](#)]
31. Delingette, H. Triangular Springs for Modeling Nonlinear Membranes. *IEEE Trans. Vis. Comput. Graph.* **2008**, *14*, 329–341. [[CrossRef](#)]
32. Mohamed, A.-N.A.; Shabana, A.A. A nonlinear visco-elastic constitutive model for large rotation finite element formulations. *Multibody Syst. Dyn.* **2011**, *26*, 57–79. [[CrossRef](#)]
33. Shan, M.; Guo, J.; Gill, E. Contact dynamic models of space debris capturing using a net. *Acta Astronaut.* **2017**, *158*, 198–205. [[CrossRef](#)]
34. Zhang, F.; Huang, P.; Meng, Z.; Zhang, Y.; Liu, Z. Dynamics Analysis and Controller Design for Maneuverable Tethered Space Net Robot. *J. Guid. Control Dyn.* **2017**, *40*, 1–16. [[CrossRef](#)]

35. Si, J. Dynamics Modeling and Simulation of a Net Closing Mechanism for Tether-Net Capture. *Int. J. Aerosp. Eng.* **2021**, *2021*, 1–16. [[CrossRef](#)]
36. Baumgarte, J.W. A New Method of Stabilization for Holonomic Constraints. *J. Appl. Mech.* **1983**, *50*, 869. [[CrossRef](#)]
37. Liu, Y. *Advanced Dynamics*; Academic: Beijing, China, 2003; p. 113.
38. Chiou, J.C.; Wu, S.D.; Wit, S.D. Constraint violation stabilization using input-output feedback linearization in multibody dynamic analysis. In Proceedings of the Guidance, Navigation, and Control Conference, San Diego, CA, USA, 29–31 July 1996.
39. Mueller, M.W.; D’Andrea, R. Stability and control of a quadcopter despite the complete loss of one, two, or three propellers. In Proceedings of the 2014 IEEE International Conference on Robotics and Automation (ICRA), Hong Kong, China, 31 May–7 June 2014.
40. Tuna, S.E. LQR-Based Coupling Gain for Synchronization of Linear Systems. *arXiv* **2008**, arXiv:0801.3390.